MATERIALS CHEMISTRY FRONTIERS

ARTICLE

Morphology Control Enables Thickness-insensitive Efficient Nonfullerene Polymer Solar Cells

Received 00th January 20xx,
Accepted 00th January 20xx

DOI: 10.1039/x0xx00000x

www.rsc.org/

Xiaoyu Liu,[ab] Long Ye,[*c] Wenchao Zhao,[b] Shaoqing Zhang,[*a] Sunsun Li,[b] Gregory M. Su[d], Cheng Wang[d], Harald Ade[*c] and Jianhui Hou[*b]

Owing to the use of cost-effective materials and excellent stability, nonfullerene polymer solar cells (PSCs) have great potential for realizing large-area industrial production. In contrast to fullerene-based devices, non-fullerene PSCs have exhibited superior photovoltaic performance with up to 12% efficiency and long-term thermal stability. Presently, one of the major factors hindering industrial production is the high sensitivity of the power conversion efficiency (PCE) to thickness variations, which can significantly affect the manufacturing yields and production costs of roll-to-roll processing. Specifically, the device fill factors and PCEs of many high-efficiency nonfullerene PSCs show a significant loss when the thickness of the active layer is over 100 nm. In order to achieve high output capabilities earlier, there is an urgent need for finding a processing method to fabricate high-efficiency thick-film nonfullerene PSCs. Controling the morphology and performance sensitivity in thick-film non-fullerene devices is a great challenge in the field. Here, we present a simple morphology optimization method via thermal annealing to fabricate highly efficient thickness-insensitive non-fullerene PSCs. After this treatment, PBDB-T/IT-M-based nonfullerene PSCs can afford an impressive PCE up to ~9.4% at an active layer thickness of 250 nm. In addition, the devices with an active layer thickness of 400 nm still maintain high efficiency close to 9%. The photovoltaic properties and morphology parameters resolved from hard and soft X-ray scattering clearly indicate that thermal annealing plays a key role in improving film thickness insensitivity for non-fullerene PSCs.

Introduction

Solution-processed bulk-heterojunction (BHJ) organic solar cells have attracted increased attention in recent years due to their great potential to make large area and flexible solar panels through low-cost solution-coating methods.[1-6] In BHJ polymer solar cells (PSCs), the active layer typically incorporates a conjugated polymeric donor and a polymeric or small molecular acceptor materials.[7-9] Most high-performance PSCs are fabricated with a thin active layer with a thickness of around 100 nm due to the relatively low carrier mobilities of the organic semiconductors. As the active layer thickness of the PSCs increases, the probability of charge recombination also increases, resulting in a reduced fill factors (FF) and consequently inferior photovoltaic performance.[10-15] Although thin-film PSCs are promising for lowering production costs, it is challenging to fabricate reproducible PSCs with precise control over commercialization processes. For large area and high-speed roll-to-roll printing, increasing the thickness of the active layer would not only absorb more solar radiation and produce higher photocurrent, but also be more tolerant of thickness variation for high quality or yield control of PSC products. Therefore, to pursue thickness-insensitive photovoltaic devices via a facile method is of great importance for large-scale production of PSCs.

Substantial progress in PCE has been achieved in thick-film polymer-fullerene PSCs mainly due to extensive efforts in improving and developing the thickness-insensitive devices for photoactive layers over 200 nm. In 2005, the Yang group fabricated a polymer-based photovoltaic device that consisted of P3HT: PCBM (1:1) with an active layer thickness of 210-230 nm and a very high FF of 67.4% and a PCE of 4.4%.[16] Subsequently, the You group reported the first successful application of fluorine to a donor–acceptor conjugated polymer, PBnDT-DTffBT, which exhibited exceptional performance (7.2% for a PBnDT-DTffBT/$PC_{61}BM$-based device with a 190 nm thick active layer) in BHJ solar cells.[17] Recently, Yan and co-workers developed a favorable polymer: fullerene morphology (containing highly crystalline and small polymer domains) in high-performance thick-film PSCs (250-300 nm) for multiple polymer: fullerene combinations. All devices yielded PCEs over 9.5% and the best combination achieved a PCE of 10.8% and fill factors up to 77%.[18] As demonstrated, more and more studies of thick film PSCs are focused on the conventional BHJ active layer based on a semi-crystalline polymer donor and a fullerene derivative acceptor.[16-26] However, there is a lack of a simple and effective processing method to improve thickness insensitivity in non-fullerene PSCs.

At present, the photovoltaic performance of PSCs based on non-fullerene acceptors has surpassed the traditional fullerene-based

[a] School of Chemistry and Biology Engineering University of Science and Technology Beijing, Beijing 100083, China E-mail: shaoqingz@ustb.edu.cn
[b] State Key Laboratory of Polymer Physics and Chemistry, Beijing National Laboratory for Molecular Sciences, Institute of Chemistry, Chinese Academy of Sciences, Beijing 100190, P. R. China. hjhzlz@iccas.ac.cn
[c] Department of physics, North Carolina State University, Raleigh, North Carolina 27695, United States E-mail: hwade@ncsu.edu; lye4@ncsu.edu
[d] Advanced Light Source, Lawrence Berkeley National Laboratory, Berkeley, CA, USA

† Electronic Supplementary Information (ESI) available: additional characterization data. See DOI: 10.1039/x0xx00000x

PSCs.[27-36] Compared with fullerene acceptors, non-fullerene acceptors have attracted much attention because of their outstanding absorption properties, easily tunable energy levels, and promise for compatibility with high-throughput roll-to-roll printing.[37-42] However, the majority of fullerene-free PSCs have optimum PCEs with active layer thicknesses of 100 nm or less. For example, our group demonstrated PBDB-T: ITIC-based fullerene-free PSCs with outstanding PCEs of up to 11.21%, and the optimal thickness is 100 nm.[43, 44] Our group also rationally designed a new non-fullerene acceptor (IT-M in **Figure 1**) with superior photovoltaic performance. For the PBDB-T: IT-M devices, the highest PCE among single-junction laboratory-scale PSCs was 12.05%. [5] Importantly, the Li group fabricated a non-fullerene PSC with a high PCE of 11.77% by using m-ITIC as an acceptor and a medium band gap conjugated polymer, J61, as a donor, and the performance showed less thickness dependence.[45] As has been demonstrated in earlier studies, most of the record-performing non-fullerene PSCs were obtained at an optimal thickness of ~100 nm, while the thickness-dependent behavior of nonfullerene PSCs have not been well studied and explored in terms of molecular packing, mesoscale morphology, and charge transport. Thus, it is very important and meaningful to develop a simple morphology optimization method which could maintain high PCEs across a range of film thickness in the non-fullerene PSCs.

In this contribution, we present thermal annealing as a simple morphology optimization method to promote the device performance of thick-film non-fullerene PSCs. These devices are based on PBDB-T (poly[(2,6-(4,8-bis(5-(2-ethylhexyl)thiophen-2-yl)-benzo[1,2-b:4,5-b']dithiophene))-alt-(5,5-(1',3'-di-2-thienyl-5',7'-bis(2-ethylhexyl)benzo[1',2'-c:4',5'-c']dithiophene-4,8-dione))]): IT-M and a regular device configuration of ITO (indium tin oxide)/PEDOT: PSS/PBDB-T: IT-M(1:1, w/w)/PFN-Br/Al (see **Figure 1a** and **1b**). Encouragingly, a high PCE of up to 9.37% was achieved (82% of the optimum value at ~100 nm) with an active layer thickness of ~250 nm. Moreover, PBDB-T: IT-M devices still reach a PCE of nearly 9% (77% of the optimum value) when the thickness of the active layer is close to 400 nm. Detailed morphology and charge transport studies suggest efficient charge transport, ordered packing and relatively high domain composition variations in non-fullerene systems collectively afford such high PCEs in thick-film devices after thermal annealing. Our findings indicate that the formation of efficient photovoltaic blends with a thick active layer is not limited to fullerene-based systems. Our morphology control approach sould be applicable to other polymer: non-fullerene systems to fabricate nearly thickness-insensitive devices.

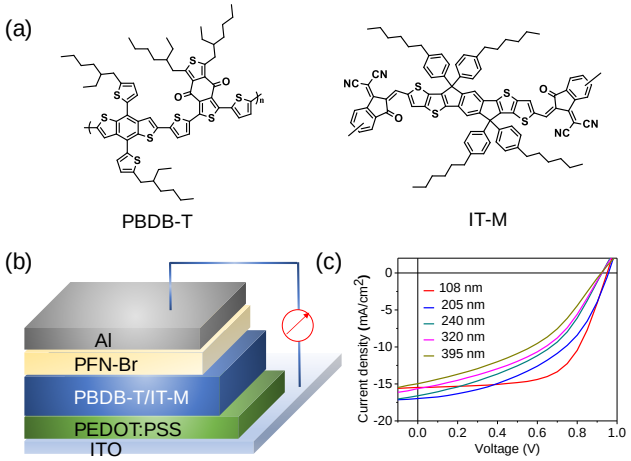

Figure 1. a) Chemical structures of PBDB-T and IT-M; b) Device configuration of non-fullerene PSCs; c) J-V curves of as-cast PBDB-T:IT-M devices as a function of active layer thickness.

Results and discussion

Annealing promotes ordering

We first examined the characteristics of devices that were prepared with PBDB-T: IT-M with varying active layer thickness. The current density-voltage (J-V) curves under the illumination of AM 1.5G 100 mW/cm^2 are shown in **Figure 1c**. The thick-film devices show a dramatic reduction in both FF and PCE compared to the control devices (~100 nm active layer). For roll-to-roll solution-processing of BHJ PSCs, a large loss of photovoltaic performance resulting from thick active layers would be unfavourable. Ultraviolet–visible (UV–vis) absorption spectra of as-cast and annealed films are presented in **Figure 2**. In comparison to the as-cast devices, the absorption spectra of thermally annealed devices show a slight red-shift. Moreover, a significant increase in the intensity of the characteristic absorption peak (~700 nm) of IT-M is observed for the annealed blend films, indicating that thermal annealing most likely influences the ordering of the small molecule acceptor in this blend system. Therefore, we introduce thermal annealing as a simple method for the morphology optimization of the PBDB-T: IT-M films.

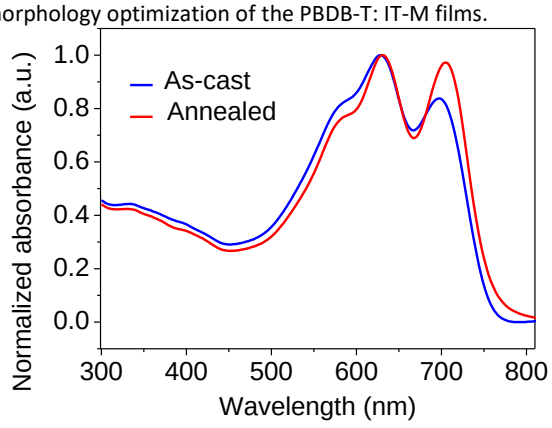

Figure 2. UV-vis absorption spectra of as-cast and annealed PBDB-T: IT-M blend films with a thickness of ~250 nm.

Thickness-dependent Photovoltaic properties

To study the thickness dependence of the photovoltaic performance of PBDB-T:IT-M-based non-fullerene PSCs, we fabricated the devices under optimal processing conditions while varying the thickness of the active layer. A regular device configuration of ITO (indium tin oxide)/PEDOT: PSS/PBDB-T: IT-M (1:1, w/w)/PFN-Br/Al was utilized in this work. The active layers with different thickness were prepared in two varieties: as-cast and post-cast thermally annealed. The processing parameters such as D/A ratio (w/w), additive ratio (v/v), spin coating rate were systematically investigated to obtain the optimal device performance based on PBDB-T:IT-M system. Here, chlorobenzene was selected as host solvent to fabricate thick-film PSCs with an optimal D/A ratio of 1:1 and 1% (vol) of 1,8-diiodoctane as the additive. The photovoltaic performances of the thick-film PSCs were measured under illumination of AM 1.5G simulated solar light at 100 mW/cm^2 and the detailed photovoltaic parameters are summarized in **Table 1**. The corresponding *J-V* curves are shown in **Figure 4a** and **Figure S1**. As shown in **Figure 3**, the PCE and FF values of as-cast and annealed devices are plotted as a function of the thickness of the active layer. Among the device parameters, we noticed the significant loss in PCE for thick-film devices is mainly due to a large drop in the FF. For instance, the FF is significantly decreased by ~1/3 in the as-cast devices when the thickness of the active layer increases from ~100 nm to ~250 nm. After the thermal annealing treatment, the thickness dependence of the PCE and FF for the annealed devices is reduced relative to the as-cast devices.

We examined ~250 nm-thick non-fullerene devices to amplify the morphology-performance relations, as the best-performing thick-film (over 200 nm) devices were achieved at a thickness of ~250 nm (see **Figure 4a**). With thermal annealing (100 °C), the thick-film PSCs based on PBDB-T: IT-M displayed a V_{oc} of 0.95 V, a J_{sc} of 18.13 mA/cm^2, and a FF of 0.54, yielding a high PCE of 9.37%. While for the as-cast devices without thermal annealing, the thick-film PSCs showed a lower PCE of 6.73% along with a decreased V_{oc} of 0.92 V, a J_{sc} of 16.60 mA/cm^2, and a low FF of 0.44. Furthermore, we fabricated thick-film PSCs with a larger device area of 1.00 cm^2, and the photovoltaic parameters of the best device shows a V_{oc} of 0.93 V, a J_{sc} of 17.4 mA/cm^2, and a FF of 0.51, resulting in a PCE of 8.28% (see Figure S3). The external quantum efficiency (EQE) curves of the two thick-film PSCs are displayed in **Figure 4b**. Clearly, the thermally annealed devices show higher EQE values in the wavelength region of 300–750 nm, which is consistent with their higher J_{sc}. To understand the charge recombination of the thick-film PBDB-T:IT-M-based devices, we measured the dependence of J_{sc} as a function of light intensity (P_{light}) (**Figure 4c**). Generally, a linear dependence of log (J_{sc}) and log (P_{light}) with a slope close to 1 suggests weak bimolecular recombination in the PSCs, whereas a slope far less than 1 indicates partial loss of charge carriers due to bimolecular recombination between free holes and electrons during charge transport. Compared with the as-cast device, the fitted slope (S) of annealed device is almost the same (0.97) within the experimental error.[46, 47] These results suggest that bot as-cast and annealed thick-film PBDB-T: IT-M based PSCs have similar charge recombination behavior. The exciton dissociation probabilities (P_{diss}) of these two kinds of devices were measured and analyzed by the curves of photo-generated current density (J_{ph}) versus effective voltage (V_{eff}). As shown in **Figure 4d**, under short-circuit conditions, according to the equation $P_{diss} = J_{ph}/J_{sat}$ (J_{sat} represents the saturation photocurrent density), the exciton dissociation probability was calculated to be 90.71% for as-cast devices and 91.9% for the thermally annealed devices. This means PBDB-T: IT-M based devices with thermal annealing are more beneficial for exciton dissociation and charge creation.

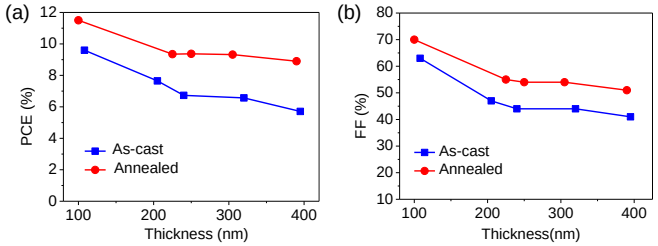

Figure 3. Plots of PCE (a) and FF (b) as a function of the active layer thickness for PBDB-T/IT-M BHJ solar cells under different conditions (as-cast and thermal annealing).

To further explore the influence of thermal annealing on the charge transport properties of thick films, the space-charge-limited (SCL) hole and electron mobilities were measured with a device structure of ITO/PEDOT: PSS /active layer/Au and ITO/ZnO/active layer/Al, respectively.[48] As shown in **Figure S4**, the hole mobility (μ_h) and electron mobility (μ_e) of PBDB-T/IT-M based as-cast devices are 1.87 ×10^{-4} cm^{2}V^{-1}s^{-1} and 1.22 ×10^{-4} cm^{2}V^{-1}s^{-1} with μ_h/μ_e of 1.53. In contrast, the devices with thermal annealing exhibit higher hole and electron mobilities (2.74 × 10^{-4} cm^{2}V^{-1}s^{-1} and 2.06 × 10^{-4} cm^{2}V^{-1}s^{-1} with μ_h/μ_e of 1.33). We also found that the electron mobility of pure acceptor was significantly increased from 2.17×10^{-5} cm^{2}V^{-1}s^{-1} to 2.20×10^{-4} cm^{2}V^{-1}s^{-1} after thermal annealing. The higher carrier mobility in the active layer of annealed devices relative to as-cast devices resulted in the higher J_{sc} value for the corresponding PSCs. In contrast with fullerene-based thick-film devices, non-fullerene systems commonly show a reduction in charge carrier mobilities of almost one or two orders of magnitude.[49-51] Here, we interpret these results as following: the improved carrier transport helps alleviate the accumulation of photo-generated carriers in thick-film devices, which decreases the probability of carrier recombination and consequently enhances the carrier collection efficiency.[52-54]

It is known that thicker films can enhance light absorption, while we still cannot achieve higher PCE due to the decrease of the FF when the active layer thickness is over 100 nm.[55, 56] Due to the increased carrier diffusion length, more and more charge recombination will occur in the active layer. Presently, PSC systems still face a severe challenge to achieve efficient charge carrier transport and suppress recombination in thick-films. For thick-film non-fullerene PSCs based on PBDB-T:IT-M, thermal annealing can obviously maintain reasonable good FF and enhance the J_{sc} as the active layer thickness increased up to 400 nm. (See **Figure S1**). In contrast, as shown in **Table S1**, the photovoltaic performance of the as-cast devices decreased with the increase of active layer thickness. Our results suggest that thermal annealing is a good candidate as a processing

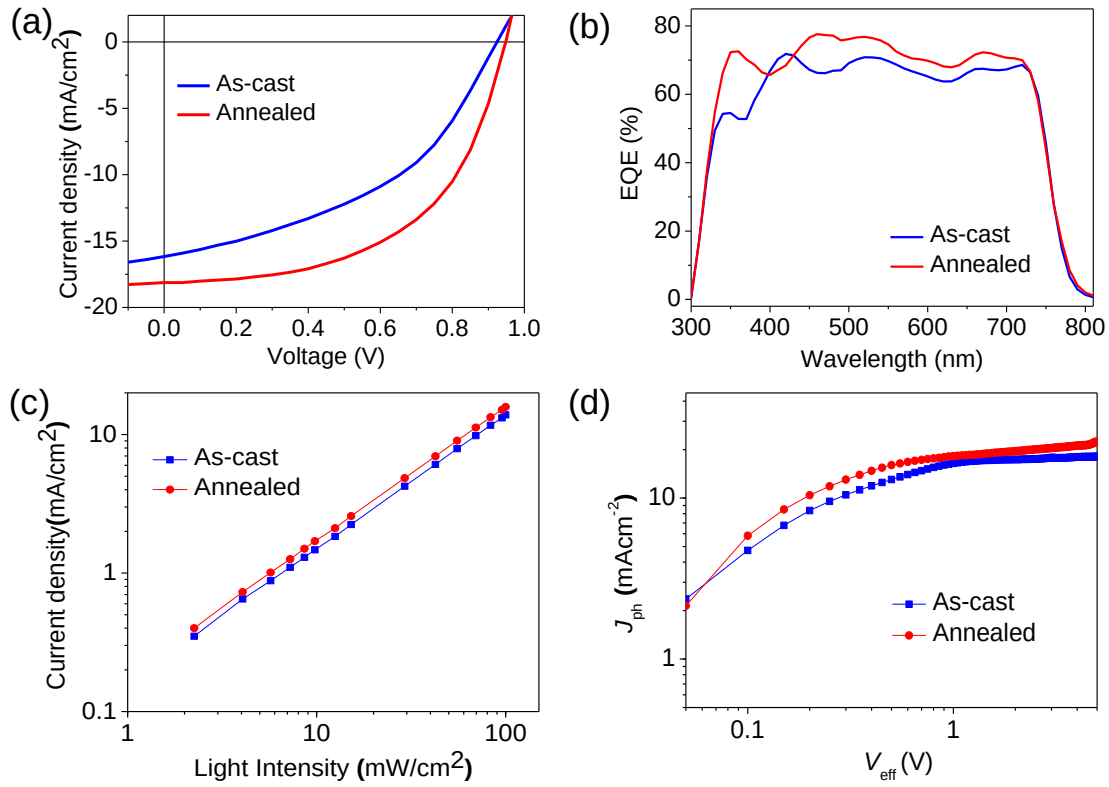

Figure 4. The best-performing thick-film PBDB-T/IT-M solar cells for as-cast and annealed devices: a) J–V curves; b) EQE curves; c) Plot of J_{SC} vs light intensity; d) J_{ph} versus V_{eff} plots.

Table 1. Statistical data of as-cast devices and photovoltaic properties of annealed PBDB-T/IT-M (1:1) based BHJ solar cells fabricated with different active layer thicknesses.

Conditions	V_{oc} (V)	J_{sc} (mA/cm^2)	FF (%)	PCE[a] (%)	Thickness (nm)
As-cast	0.924±0.01	16.60±0.16	0.44±0.02	6.59±0.14 (6.73)	240
Annealed	0.930±0.01	9.90±0.23	0.68±0.01	6.15±0.13 (6.28)	50
	0.961±0.01	16.69±0.13	0.70±0.02	11.34±0.16(11.50)	100
	0.940±0.01	18.17±0.20	0.55±0.03	9.13±0.22 (9.35)	225
	0.948±0.01	18.13±0.17	0.54±0.03	9.14±0.23 (9.37)	250
	0.943±0.01	18.44±0.15	0.54±0.01	9.15±0.17 (9.32)	305
	0.942±0.01	18.66±0.12	0.51±0.02	8.80±0.10 (8.90)	390

[a] The reported data are the average PCEs from ten devices.

step to improve thickness-insensitivity for the large area and high-speed roll-to-roll production of non-fullerene PSCs.

Surface Morphology and Molecular Packing for thick-films

To understand the morphology in real-space, we used tapping-mode atomic force microscopy (AFM) and transmission electron microscopy (TEM) to analyze the annealed and as-cast thick-film (~250 nm) devices. According to the AFM results (see **Figure 5a** and **5b**), the two blend films show very similar surface topography, and the root-mean-square roughness (R_q) values of the two films are 1.93 nm and 2.11 nm, respectively. As shown in the AFM phase images (**Figure S5**) of the two blend films, features of phase separation are clearly observed. In the TEM measurements, the two films also exhibit phase-separated morphologies (see **Figure S6**), which may be advantageous for realizing efficient exciton dissociation in the device. Based on the AFM and TEM observations, we were not able to quantitatively compare the length scale of phase separation between as-cast and annealed thick-film devices. Considering that AFM cannot reflect the bulk structure and morphology of the active layers in detail, we further analyzed thin films with synchrotron radiation-based techniques including grazing incidence wide-angle X-ray scattering (GIWAXS) and resonant soft X-ray scattering (R-SoXS). GIWAXS and R-SoXS were performed at beamlines 7.3.3 and

11.0.1.2, respectively, at the Advanced Light source (ALS), Lawrence Berkeley National Lab.

GIWAXS was used to investigate the molecular packing and crystalline texture in the thick films with and without thermal treatment.[57] From the 2D patterns and 1D line profiles (see **Figure 5c-5d** and **Figure S7**), the annealed thick-film shows a slightly higher scattering intensity although the features/peaks in out-of-plane (OOP) directions in both as-cast and annealed films are very similar. The π-π coherence length in the OOP direction is a key measure of ordering in organic semiconductor materials and often related to charge transport in devices. We note that the OOP (010) peaks of the donor and acceptor have some overlap, and we deconvoluted the individual contributions via multi-peak fitting with Gaussian peaks.

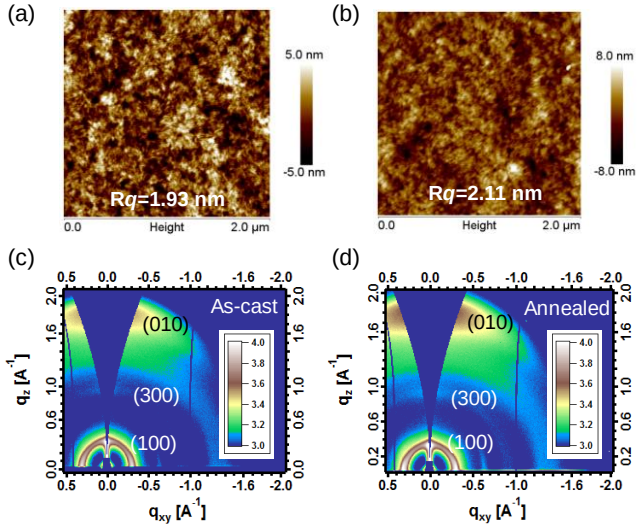

Figure 5. Tapping mode AFM topography of PBDB-T/IT-M based thick-film devices with (a) annealing treatment and (b) as-cast treatment; c,d) 2D GIWAXS patterns of as-cast and annealed PBDB-T:IT-M thick-films (~250 nm).

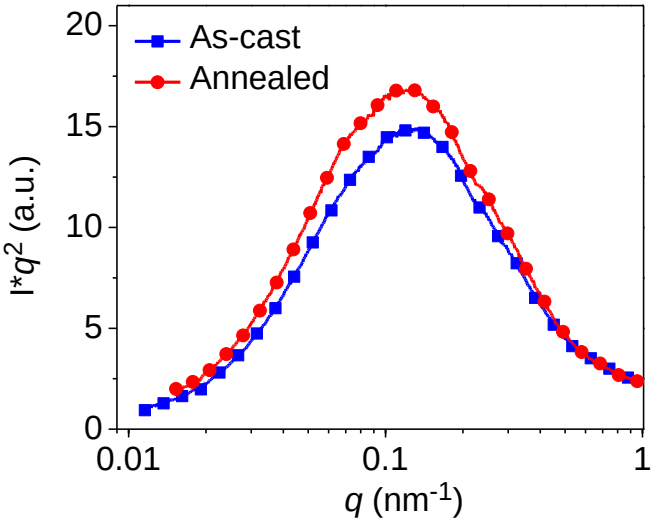

Figure 6. Thickness normalized and Lorentz-corrected R-SoXS profiles of the as-cast and annealed PBDB-T: IT-M thick-films.

We find that both of the OOP π-π coherence lengths of the small molecular acceptors (SMAs) (L_A) and the polymer donor (L_D) are increased after annealing (see **Table 2**). We rationalized that thermal annealing provides sufficient driving forces for the polymer and SMA molecules to reorganize. The change of molecular ordering upon annealing is schematically shown in Figure S8. It is expected that charge transport improves with increasing π-π coherence length. Therefore, the improved OOP π-π coherence lengths of SMA indicates the higher ordering of SMA in the thick film after thermal annealing. This may be a key factor that partially contributes to higher J_{sc} and FF. This observation also agrees well with our recent studies[58].

Bulk Morphology for thick-films

Resonant soft X-ray scattering (R-SoXS) was applied to analyze the domain spacing and average composition variation (average domain purity) of the thick-films. The soft X-ray energy was tuned between 270 and 300 eV in transmission R-SoXS experiments. Here, we select an X-ray energy of 283.8 eV to enhance the material contrast. From the scattering profiles plotted in **Figure 6**, the two blends films exhibit similar length-scale features and a long period (center-to-center domain spacing) of ~50 nm was obtained under the assumption of a globally isotropic 3D morphology. Following our previous analysis[59, 60], the average composition variation (ACV) of an organic blend film is proportional to the square-root of the normalized integrated scattering intensity (ISI). Thus, ISI is a measure of the average domain purity over the full *q* range probed. Here, we found that the relative domain purity is improved by 4.2% after annealing. A higher domain purity can aid efficient charge creation[61] and improve the device FF. Recently, we found that the PBDB-T: IT-M system is likely[62] a lower critical solution temperature (LCST) system (interaction parameter χ scales with -1/T). Here, this inference is verified experimentally by explicit miscibility measurements following previously established protocols[63] (see **Figure S9**). We note that annealing at ~150 ˚C is a temperature where the residual IT-M in the mixed polymer-rich domains is ~24% and thus close to the percolation threshold[64], a composition that is likely optimal in terms of the balance between charge creation (J_{SC}) and charge recombination (FF).

Table 2. Morphological parameters of as-cast and annealed PBDB-T/IT-M devices with thick-films (~250 nm).

Blends	L_D (nm)	L_A (nm)	Long Period (nm)	Relative ACV
As-cast	1.79	3.29	51.1	0.96
Annealed	1.89	3.74	53.5	1

Generally, higher χ parameter enables larger average domain purity and higher scattering intensity. Therefore, a higher processing temperature may induce a higher domain purity compared to as-cast devices processed at room temperature.[5] In addition, the strong relation observed here is in line with the FF-ACV correlations shown in our prior studies of thin-film devices[60, 62, 65]. These studies suggest optimizing the molecular ordering and average composition variation is key to achieving high-efficiency in non-fullerene PSC devices.

Conclusions

In summary, we have systematically studied the molecular ordering, mesoscale morphology, and charge recombination in thick-film non-fullerene PSCs based on a high-performance PBDB-T/IT-M system. We found thermal annealing can be very useful to boost the performance of thick-film PBDB-T/IT-M devices. A high PCE of 9.37% was obtained from PBDB-T: IT-M devices with a film thickness of 250 nm and the devices can maintain a high efficiency of ~9% when the thickness of the active layer is increased to 400 nm. UV-vis absorption, SCLC mobility, and morphology studies show that the electron mobility of IT-M becomes higher and the blend films possess more ordered packing and higher average domain purity after thermal annealing. Consequently, these factors improve the charge creation and transport, and thus lead to improved thickness insensitivity of device performance. We note that the photovoltaic performance in our thick-film devices is still limited by the carrier mobility. It will be more advantageous to improve the efficiency of thick film devices if the carrier mobility is improved via future molecular design and device engineering. These results reveal the critical morphological parameters that determine photovoltaic performance in thick-film devices. This work highlights the importance of controlling molecular ordering and phase separation in achieving high-efficiency thick-film non-fullerene PSC devices, which will be beneficial for commercial roll-to-roll printing technology.

Experiments

Fabrication of the polymer solar cells

PBDB-T[35] and IT-M[5] were synthesized as described in our previous works. The PSCs devices were fabricated with a traditional device configuration of ITO (indium tin oxide)/PEDOT:PSS/PBDB-T:IT-M (1:1, w/w)/PFN-Br/Al. At first, the ITO-coated glass substrates were cleaned sequentially by using detergent, deionized water, acetone, and isopropanol. Then UV/ozone treatment was performed on the ITO glasses for 20 minutes. A thin layer (nearly 30 nm) of poly(3,4-ethylenedioxythiophene):poly(styrene sulfonate) (PEDOT:PSS) (Heraeus Materials, 4083) was spin coated onto the cleaned ITO surface, and the ITO substrates were annealed in air at 150 ^{o}C for 15 minutes. The active-layer solution of PBDB-T: IT-M (1:1, wt/wt) were prepared in chlorobenzene, and the solution was stirred on a hot plate at 40 ^{o}C for at least 5 h. The concentration of PBDB-T: IT-M blend solution concentration (based on the weight of the polymer) was 10 mg/mL. 1% vol solvent additive (1, 8-diiodoctane) was added into the blend solution before the spin coating process. After spin coating the active layer on to the PEDOT: PSS, the devices adopted two different processing method (with and without thermal annealing) to optimize the morphology of the blend films. Next, a 5 nm thin PFN-Br was spin-coated on the top of the active layer. Then, the device fabrications were completed by vacuum evaporating Al metal electrode. Except for the spin coating of PEDOT: PSS, the other processes was conducted inside the glove box under the condition of nitrogen atmosphere.

Device Measurements

The device current–voltage curves were measured under AM 1.5G (100 mW/cm^2) using a Class AAA solar simulator (XES-70S1, SAN-EI Electric Co., Ltd). The light intensity was calibrated to obtain spectral mismatch to unity via a standard photovoltaic cell (with a KG5 filter). The effective area of devices is 4.03 mm^2, which is defined by using the metal mask aligned with an aperture. All EQE data were measured by using a solar cell spectral response measurement system (QE-R3011, Enli Technology Co. Ltd), which was equipped with a standard silicon solar cell. The film thickness data were determined using a surface profilometer (Dektak XT, Bruker). The SCLC measurements for PBDB-T: IT-M devices were measured in the configuration of ITO/PEDOT: PSS /active layer (200 nm)/Au for hole-only devices and ITO/ZnO/active layer (200 nm)/Al for electron-only devices. The light-dependent tests for PBDB-T: IT-M devices were measured by inserting neutral density filters to tune the light intensity during J-V testing. The nanoscale morphology of blend films was measured by using Veeco Nanoscope V atomic force microscopy (AFM) in tapping mode. The transmission electron microscopy (TEM) characterization was carried out using a JEOL 2200FS instrument with an accelerating voltage of 160 kV. All film samples were spin cast on PEDOT:PSS coated indium tin oxide (ITO) substrates.

X-ray scattering measurements

The GIWAXS[66] and near edge X-ray absorption fine structure spectroscopy (NEXAFS)[67] experiments were respectively done at beamline 7.3.3 and 5.3.2.2 at the ALS. Resonant soft X-ray scattering (R-SoXS)[68] was performed in transmission geometry with linearly polarized photons under high vacuum (1×10^{-7} Torr) at beamline 11.0.1.2 at the Advanced Light Scattering (ALS), and the scattering 2D images were recorded by an in-vacuum cooled (-45 ^{o}C) CCD detector (Princeton Instruments, PI-MTE, 2048 pixels×2048 pixels). Azimuthally averaged 1-D I(q)-q profiles can be obtained by the reduction of 2D images using a custom Nika analysis package implemented within Igor and subsequently normalized for the instantaneous X-ray flux.

Acknowledgements

We acknowledge the financial support of the Ministry of Science and Technology of China (2014CB643501), NSFC (21325419, 91333204, 21604017 and 51373181), and the Chinese Academy of Sciences (XDB12030200, KJZD-EW-J01). L. Ye and H. Ade were supported by the ONR grant N00141512322 and a University of North Carolina General Administration Research Opportunity Initiative (ROI) grant. X-ray data were acquired at beamlines 11.0.1.2, 7.3.3, and 5.3.2.2 at the Advanced Light Source, LBNL, which is supported by the Director, Office of Science, Office of Basic Energy Sciences, of the U.S. Department of Energy under Contract No. DE-AC02-05CH11231. C. Zhu, A.L.D. Kilcoyne, Y. Yu, and E. Schaible are appreciated for the beamline maintenance.

Notes and references

1. J. Zhao, Y. Li, J. Zhang, L. Zhang, J. Y. L. Lai, K. Jiang, C. Mu, Z. Li, C. L. C. Chan and A. Hunt, *Journal of Materials Chemistry A*, 2015, **3**, 20108-20112.
2. G. Yu, J. Gao, J. C. Hummelen, F. Wudl and A. J. Heeger, *Science*, 1995, **270**, 1789-1791.
3. C. J. Brabec, N. S. Sariciftci and J. C. Hummelen, *Advanced Functional Materials*, 2001, **11**, 15–26.

4. R. Søndergaard, M. Hösel, D. Angmo, T. T. Larsen-Olsen and F. C. Krebs, *Materials Today*, 2012, **15**, 36-49.
5. S. Li, L. Ye, W. Zhao, S. Zhang, S. Mukherjee, H. Ade and J. Hou, *Advanced materials*, 2016, DOI: 10.1002/adma.201602776.
6. L. Ye, Y. Xiong, H. Yao, A. Gadisa, H. Zhang, S. Li, M. Ghasemi, N. Balar, A. Hunt, B. T. O'Connor, J. Hou and H. Ade, *Chemistry of Materials*, 2016, **28**, 7451-7458.
7. W. Jiang, L. Ye, X. Li, C. Xiao, F. Tan, W. Zhao, J. Hou and Z. Wang, *Chemical Communications*, 2014, **50**, 1024-1026.
8. L. Lu, T. Zheng, Q. Wu, A. M. Schneider, D. Zhao and L. Yu, *Chemical Reviews*, 2015.
9. J. Chen and Y. Cao, *ChemInform*, 2010, **42**, 1709-1718.
10. M. Shin, H. Kim, J. Park, S. Nam, K. Heo, M. Ree, C. S. Ha and Y. Kim, *Advanced Functional Materials*, 2010, **20**, 748-754.
11. W. Ma, C. Yang, X. Gong, K. Lee and A. J. Heeger, *Advanced Functional Materials*, 2005, **15**, 1617-1622.
12. Y. Y. Lee, K. H. Tu, C. C. Yu, S. S. Li, J. Y. Hwang, C. C. Lin, K. H. Chen, L. C. Chen, H. L. Chen and C. W. Chen, *Acs Nano*, 2011, **5**, 6564-6570.
13. H. Kim, M. Shin and Y. Kim, *Journal of Physical Chemistry C*, 2009, **113**, 1620-1623.
14. S. R. Mi, H. J. Cha and J. Jin, *Current Applied Physics*, 2010, **10**, S206–S209.
15. J. Peet, J. Y. Kim, N. E. Coates, W. L. Ma, D. Moses, A. J. Heeger and G. C. Bazan, *Nat Mater*, 2007, **6**, 497-500.
16. G. Li, V. Shrotriya, J. Huang, Y. Yao, T. Moriarty, K. Emery and Y. Yang, *Nature Materials*, 2005, **4**, 864-868.
17. H. Zhou, L. Yang, A. C. Stuart, S. C. Price, S. Liu and W. You, *Angewandte Chemie*, 2011, **50**, 2995-2998.
18. Y. Liu, J. Zhao, Z. Li, C. Mu, W. Ma, H. Hu, K. Jiang, H. Lin, H. Ade and H. Yan, *Nat Commun*, 2014, **5**, 5293.
19. W. Li, K. H. Hendriks, W. S. C. Roelofs, Y. Kim, M. M. Wienk and R. A. J. Janssen, *Advanced Materials*, 2013, **25**, 3182-3186.
20. N. Gasparini, L. Lucera, M. Salvador, M. Prosa, G. D. Spyropoulos, P. Kubis, H.-J. Egelhaaf, C. J. Brabec and T. Ameri, *Energy Environ. Sci.*, 2017, DOI: 10.1039/c6ee03599j.
21. A. Armin, M. Hambsch, P. Wolfer, H. Jin, J. Li, Z. Shi, P. L. Burn and P. Meredith, *Advanced Energy Materials*, 2015, **5**, 1401221.
22. X. Zhu, J. Fang, K. Lu, J. Zhang, L. Zhu, Y. Zhao, Z. Shuai and Z. Wei, *Chemistry of Materials*, 2014, **26**, 6947-6954.
23. J. Chen, L. Zhang, X. Jiang, K. Gao, F. Liu, X. Gong, J. Chen and Y. Cao, *Advanced Energy Materials*, 2017, **7**, 1601344.
24. Z. Chen, P. Cai, J. Chen, X. Liu, L. Zhang, L. Lan, J. Peng, Y. Ma and Y. Cao, *Advanced materials*, 2014, **26**, 2586-2591.
25. J. Zhao, Y. Li, A. Hunt, J. Zhang, H. Yao, Z. Li, J. Zhang, F. Huang, H. Ade and H. Yan, *Advanced materials*, 2016, **28**, 1868-1873.
26. X. Zhu, B. Xia, K. Lu, H. Li, R. Zhou, J. Zhang, Y. Zhang, Z. Shuai and Z. Wei, *Chemistry of Materials*, 2016, **28**, 943-950.
27. L. Ye, W. Jiang, W. Zhao, S. Zhang, D. Qian, Z. Wang and J. Hou, *Small*, 2014, **10**, 4658-4663.
28. E. Zhou, J. Cong, K. Hashimoto and K. Tajima, *Advanced materials*, 2013, **25**, 6991–6996.
29. M. Schubert, D. Dolfen, J. Frisch, S. Roland, R. Steyrleuthner, B. Stiller, Z. Chen, U. Scherf, N. Koch, A. Facchetti and D. Neher, *Advanced Energy Materials*, 2012, **2**, 369-380.
30. S. Li, H. Zhang, W. Zhao, L. Ye, H. Yao, B. Yang, S. Zhang and J. Hou, *Advanced Energy Materials*, 2016, **6**, n/a-n/a.
31. C. Lee, H. Kang, W. Lee, T. Kim, K. H. Kim, Y. W. Han, W. Cheng and B. J. Kim, *Advanced materials*, 2015, **27**, 2466-2471.
32. Y. Lin, J. Wang, Z. G. Zhang, H. Bai, Y. Li, D. Zhu and X. Zhan, *Advanced materials*, 2015, **27**, 1170-1174.
33. L. Gao, Z. G. Zhang, L. Xue, J. Min, J. Zhang, Z. Wei and Y. Li, *Advanced materials*, 2016, **28**.
34. H. Li, Y. J. Hwang, B. A. Courtright, F. N. Eberle, S. Subramaniyan and S. A. Jenekhe, *Advanced materials*, 2015, **27**, 3266-3272.
35. D. Qian, W. Ma, Z. Li, X. Guo, S. Zhang, L. Ye, H. Ade, Z. A. Tan and J. Hou, *Journal of the American Chemical Society*, 2013, **135**, 8464-8467.
36. Y. Zhou, T. Kurosawa, W. Ma, Y. Guo, L. Fang, K. Vandewal, Y. Diao, C. Wang, Q. Yan and J. Reinspach, *Advanced materials*, 2014, **26**, 3767-3772.
37. Z. X, T. Z, D. B, A. Z, Z. X, B. S, L. Y, Z. D, K. B and M. SR, *Journal of the American Chemical Society*, 2007, **129**, 7246.
38. J. W. Jung, J. W. Jo, C. C. Chueh, F. Liu, W. H. Jo, T. P. Russell and A. K. Jen, *Advanced materials*, 2015, **27**, 3310-3317.
39. S. Holliday, R. S. Ashraf, A. Wadsworth, D. Baran, S. A. Yousaf, C. B. Nielsen, C. H. Tan, S. D. Dimitrov, Z. Shang and N. Gasparini, *Nature communications*, 2016, **7**, 11585.
40. Y. Zhong, M. T. Trinh, R. Chen, G. E. Purdum, P. P. Khlyabich, M. Sezen, S. Oh, H. Zhu, B. Fowler and B. Zhang, *Nature communications*, 2015, **6**, 8242.
41. H. Li, T. Earmme, G. Ren, A. Saeki, S. Yoshikawa, N. M. Murari, S. Subramaniyan, M. J. Crane, S. Seki and S. A. Jenekhe, *Journal of the American Chemical Society*, 2016, **136**, 14589.
42. S. Li, W. Liu, M. Shi, J. Mai, T. K. Lau, J. H. Wan, X. Lu, C. Z. Li and H. Chen, *Energy & Environmental Science*, 2015, **9**, 604-610.
43. W. Zhao, D. Qian, S. Zhang, S. Li, O. Inganas, F. Gao and J. Hou, *Advanced materials*, 2016, **28**, 4734-4739.
44. Y. Lin, J. Wang, Z. G. Zhang, H. Bai, Y. Li, D. Zhu and X. Zhan, *Advanced materials*, 2015, **27**, 1170-1174.
45. Y. Yang, Z. G. Zhang, H. Bin, S. Chen, L. Gao, L. Xue, C. Yang and Y. Li, *Journal of the American Chemical Society*, 2016, **138**, 15011-15018.
46. A. C. Stuart, J. R. Tumbleston, H. Zhou, W. Li, S. Liu, H. Ade and W. You, *Journal of the American Chemical Society*, 2013, **135**, 1806-1815.
47. S. R. Cowan, J. Wang, J. Yi, Y. J. Lee, D. C. Olson and J. W. P. Hsu, *Journal of Applied Physics*, 2013, **113**, 154504-154504-154509.
48. J. C. Scott, G. G. Malliaras, W. D. Chen, J. C. Breach, J. R. Salem, P. J. Brock, S. B. Sachs and C. E. D. Chidsey, *Applied Physics Letters*, 1999, **74**, 1510-1512.
49. C. E. Small, S.-W. Tsang, S. Chen, S. Baek, C. M. Amb, J. Subbiah, J. R. Reynolds and F. So, *Advanced Energy Materials*, 2013, **3**, 909-916.
50. H. Hu, K. Jiang, G. Yang, J. Liu, Z. Li, H. Lin, Y. Liu, J. Zhao, J. Zhang, F. Huang, Y. Qu, W. Ma and H. Yan, *Journal of the American Chemical Society*, 2015, **137**, 14149-14157.
51. J. W. Jung, T. P. Russell and W. H. Jo, *ACS applied materials & interfaces*, 2015, **7**, 13666-13674.

52. L. M. Chen, Z. Hong, G. Li and Y. Yang, *Advanced materials*, 2009, **21**, 1434–1449.
53. V. Shrotriya, Y. Yao, G. Li and Y. Yang, *Applied Physics Letters*, 2006, **89**, 063505-063505-063503.
54. E. C. P. Smits, S. Setayesh, T. D. Anthopoulos, M. Buechel, W. Nijssen, R. Coehoorn, P. W. M. Blom, B. d. Boer and D. M. d. Leeuw, *Advanced materials*, 2007, **19**, 734-738.
55. F. Nickel, C. Sprau, M. F. G. Klein, P. Kapetana, N. Christ, X. Liu, S. Klinkhammer, U. Lemmer and A. Colsmann, *Solar Energy Materials & Solar Cells*, 2012, **104**, 18-22.
56. A. Armin, M. Velusamy, P. Wolfer, Y. Zhang, P. L. Burn, P. Meredith and A. Pivrikas, *Acs Photonics*, 2014, **1**, 173-181.
57. A. Hexemer, W. Bras, J. Glossinger, E. Schaible, E. Gann, R. Kirian, A. Macdowell, M. Church, B. Rude and H. Padmore, 2010, **247**, 235-253.
58. S. Li, L. Ye, W. Zhao, S. Zhang, H. Ade and J. Hou, *Adv. Energy Mater.*, 2017, **7**, 1700183.
59. X. Jiao, L. Ye and H. Ade, *Adv. Energy Mater.* , 2017, DOI: 10.1002/aenm.201700084.
60. L. Ye, X. Jiao, S. Zhang, H. Yao, Y. Qin, H. Ade and J. Hou, *Advanced Energy Materials*, 2017, **7**, 1601138.
61. S. Mukherjee, X. Jiao and H. Ade, *Advanced Energy Materials*, 2016, **6**, 1600699.
62. L. Ye, W. Zhao, S. Li, S. Mukherjee, J. H. Carpenter, O. Awartani, X. Jiao, J. Hou and H. Ade, *Adv. Energy Mater.* , 2017, **7**, 1602000.
63. B. A. Collins, E. Gann, L. Guignard, X. He, C. R. McNeill and H. Ade, *Journal of Physical Chemistry Letters*, 2010, **1**, 3160-3166.
64. J. A. Bartelt, Z. M. Beiley, E. T. Hoke, W. R. Mateker, J. D. Douglas, B. A. Collins, J. R. Tumbleston, K. R. Graham, A. Amassian, H. Ade, J. M. J. Frechet, M. F. Toney and M. D. McGehee, *Advanced Energy Materials*, 2013, **3**, 364-374.
65. S. Mukherjee, C. M. Proctor, G. C. Bazan, T. Q. Nguyen and H. Ade, *Advanced Energy Materials*, 2015, **5**, 1500877.
66. A. Hexemer, W. Bras, J. Glossinger, E. Schaible, E. Gann, R. Kirian, A. MacDowell, M. Church, B. Rude and H. Padmore, *Journal of Physics: Conference Series*, 2010, **247**, 012007.
67. A. L. D. Kilcoyne, T. Tyliszczak, W. F. Steele, S. Fakra, P. Hitchcock, K. Franck, E. Anderson, B. Harteneck, E. G. Rightor, G. E. Mitchell, A. P. Hitchcock, L. Yang, T. Warwick and H. Ade, *Journal of Synchrotron Radiation*, 2003, **10**, 125-136.
68. E. Gann, A. T. Young, B. A. Collins, H. Yan, J. Nasiatka, H. A. Padmore, H. Ade, A. Hexemer and C. Wang, *Review of Scientific Instruments*, 2012, **83**, 045110.